Control of phytoplankton bloom inception in the Ross Sea, Antarctica, by Ekman restratification

Matthew C. Long,[1,2] Leif N. Thomas,[1] and Robert B. Dunbar[1]

Received 30 October 2010; revised 1 June 2011; accepted 25 October 2011; published 18 January 2012.

[1] Observations from November 2006 in the southwestern Ross Sea indicate that stratification developed in a localized fashion, proximal to upper ocean fronts. These regions were hotspots for biological productivity, exhibiting greater drawdown of CO_2 and accumulation of oxygen, indicative of enhanced photosynthesis and air-sea gas exchange. While the effect of stratification is clear, the reasons for its development was not; air temperatures were unseasonably cold, sea-ice melt and sea surface warming were not significant. By comparing a one-dimensional mixed layer model with two-dimensional numerical simulations that include horizontal density gradients characteristic of the region, it is shown that Ekman advection is critical to structuring early season stratification. Where fronts are forced by winds that oppose the surface frontal current, Ekman advection displaces lighter water over dense. As biological productivity is light limited in the Ross Sea, and thus sensitive to the depth of the mixed layer, Ekman restratification plays an important role in determining the spatial distribution and development of the annual phytoplankton bloom in the region. The presence of fronts is therefore of first-order importance to the restratification and bloom dynamics of the Ross Sea in the early spring.

Citation: Long, M. C., L. N. Thomas, and R. B. Dunbar (2012), Control of phytoplankton bloom inception in the Ross Sea, Antarctica, by Ekman restratification, *Global Biogeochem. Cycles*, *26*, GB1006, doi:10.1029/2010GB003982.

1. Introduction

[2] The global ocean has sequestered 25–35% of anthropogenic CO_2 emitted over the last 200 years, thus modulating climate by regulating atmospheric pCO_2 [*Sabine et al.*, 2004; *Canadell et al.*, 2007; *Le Quéré et al.*, 2009]. Geographically, carbon cycling dynamics in deepwater formation regions, particularly in the Southern Ocean, have the greatest effect on atmospheric CO_2 [*Ito and Follows*, 2005; *Marinov et al.*, 2006]. The Ross Sea, for instance, is situated over a broad continental shelf along the Antarctic margin and is an important site of deepwater formation [*Orsi et al.*, 2002].

[3] Modeling studies and observations have shown the Ross Sea to be an important sink for anthropogenic CO_2 [*Sandrini et al.*, 2007; *Arrigo et al.*, 2008]. The mechanics of this sink rely on temporal coordination of high rates of net primary productivity (NPP) during summer, and inhibition of gas exchange by sea ice during winter [*Sweeney*, 2003; *Arrigo et al.*, 2008]. Sea ice clears from the region annually, exposing surface water to the atmosphere for a period of time between November and February. The annual expansion of the Ross Sea 'polynya' coincides with the development of a large phytoplankton bloom [*Arrigo and van Dijken*, 2004]. NPP consumes nutrients and effectively lowers the partial pressure of CO_2 in the surface ocean (pCO_2^{sw}) below that of atmospheric saturation [*Bates et al.*, 1998; *Sweeney et al.*, 2000; *Sweeney*, 2003; *Long et al.*, 2011]. On a seasonal basis, the time-integrated atmosphere-ocean flux of CO_2 is directly related to the quantity of carbon fixed by NPP [*Arrigo and van Dijken*, 2007; *Long et al.*, 2011]. Thus, the processes regulating the magnitude and variability of NPP in the Ross Sea are of primary importance to determining the region's performance as a carbon sink.

[4] Macronutrients (nitrogen, phosphorus, and silica) are typically replete in Ross Sea surface waters year-round. The availability of light and iron, therefore, are first order controls on rates of NPP. While the mechanisms controlling iron distributions in the Ross Sea are not entirely well understood, deep mixing and remineralization over winter are thought to replenish upper ocean iron concentrations; thus, iron limitation is most likely to occur when seasonally-integrated export depletes the initial inventory and exceeds rates of iron supply. Iron availability, therefore, primarily regulates bloom termination and net seasonal production across the Ross Sea [*Sedwick et al.*, 2000; *Arrigo et al.*, 2003; *Tagliabue and Arrigo*, 2005].

[5] Light limitation, by contrast, can be pronounced in the Ross Sea spring. The water column tends to be weakly stratified due to surface cooling, ice formation and convection during winter. In the absence of wind-forcing, weak stratification does not preclude the development of a spring phytoplankton bloom, since waters tend to be clear and light can penetrate deeply [*Townsend et al.*, 1992]. However, when the ocean is forced by strong winds, as is characteristic

[1]Department of Environmental Earth System Science, Stanford University, Stanford, California, USA.
[2]Now at National Center for Atmospheric Research, Boulder, Colorado, USA.

0886-6236/12/2010GB003982

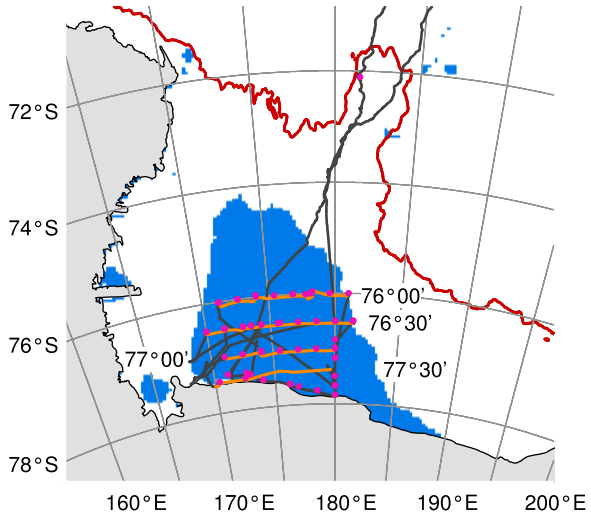

Figure 1. Cruise track (black line), CTD stations (purple dots), and main transects discussed in this paper (highlighted in orange). Background color shows sea ice presence/absence (blue = open water) for 23–26 November 2006, the time interval during which the 76°30′S line was occupied. Sea ice presence was computed from SSM/I brightness temperatures using the algorithm of *Markus and Burns* [1995]. Dark red line shows the 1000-m isobath.

of the Antarctic spring, weak stratification results in deep mixed layers (ML). Light availability is reduced as phytoplankton cells are mixed to depth in the water column; thus, rates of NPP and the onset of the spring phytoplankton bloom are sensitive to processes controlling ML depths. The ability to predict the evolution of ML depths in early spring is critical to understanding the early season evolution of phytoplankton blooms [*Lévy et al.*, 2000], particularly in light-limited settings such as the Ross Sea.

[6] Traditional models attribute variability in ML depths to one-dimensional (1-D), vertical processes, driven by air-sea fluxes of momentum, heat, and salt (freshwater). In these models, wind-driven turbulence or convection promotes ML deepening, in competition with surface freshening or warming that results in ML shoaling [e.g., *Kraus and Turner*, 1967; *Price et al.*, 1986; *Large et al.*, 1994]. One-dimensional models capture many characteristic seasonal and diurnal fluctuations in ML depths; however, they break down at ocean fronts: regions where horizontal gradients in density are large. In these regions, horizontal flows induced by eddies or ageostrophic processes can result in displacement of light water over more dense—a process that can restratify the upper ocean at rates exceeding those associated with air-sea fluxes [e.g., *Jones and Marshall*, 1997; *Oschlies*, 2002; *Fox-Kemper et al.*, 2008; *Thomas et al.*, 2008]. Furthermore, variable wind-forcing, and its orientation with respect to the direction of frontal currents, can generate transient mixing and restratification events [*Franks and Walstad*, 1997; *Thomas and Ferrari*, 2008]. This process has been shown to modulate the spatial and temporal dynamics of midlatitude, nutrient-limited, frontal blooms [*Franks and Walstad*, 1997].

[7] Since the onset of a spring bloom can be sensitive to ML depths, dynamical restratification mechanisms may play a critical role in controlling the timing of bloom inception, prior to the initiation of seasonal stratification [*Lévy et al.*, 1999, 2000]. Do such processes play a role in the Ross Sea? This region is characterized by several distinct water masses, the boundaries between which can delineate fronts. High Salinity Shelf Water (HSSW) is produced by cooling and brine rejection adjacent to the continent, predominantly on the western portion of the continental shelf [*Orsi and Wiederwohl*, 2009]. Circumpolar deepwater, Modified Circumpolar Deepwater (MCDW), and Antarctic Surface Water, each of lower density than HSSW, flow cyclonically and westward onto the shelf, entrained in the Ross Sea gyre [*Orsi and Wiederwohl*, 2009]. The juxtaposition of these water masses in the central Ross Sea gives rise to a zonal density gradient. Strong winds during the Antarctic spring lead to the opening of the Ross Sea polynya and force the exposed ocean with significant heat and momentum fluxes [*Kwok*, 2005]. The combination of lateral density gradients and winds suggests that the upper ocean of the Ross Sea is susceptible to restratification by horizontal flows near fronts.

[8] In this paper, we describe observations from the Ross Sea collected in the spring of 2006. These data show a correspondence between locations of density fronts and regions of enhanced upper-ocean stratification. Biomass and oxygen accumulation as well as CO_2 drawdown are most intense at these locations. Using idealized models, we examine the factors contributing to the development of stratification, including surface heating, ice melt, and horizontal advection of buoyancy. We make explicit comparisons between 1-D and two-dimensional (2-D) model configurations to determine the impact lateral gradients and horizontal advection have on stratification, NPP, and air-sea exchange. The results of these simulations and our data indicate that lateral processes—specifically Ekman advection—significantly affect early season restratification and thus control the evolving spatial structure of the annual phytoplankton bloom and air-sea exchange.

2. Observations

2.1. Methods

[9] Conductivity, temperature, depth (CTD) casts, underway meteorological, and sea surface observational data were collected within the Ross Sea continental shelf (south of 70°S) aboard the *R/V Nathaniel B. Palmer* between 11 November and 5 December 2006 (cruise NBP06-08; Figure 1).

[10] A total of 71 CTD casts were collected over the continental shelf during NBP06-08. In this paper, we present CTD-cast observations of salinity, temperature, and dissolved oxygen. Salinity samples were analyzed at 24°C using a Guildline 8400 Autosal four-electrode salinometer at sea. Autosal bottle salinity values were used to assess the performance of both CTD conductivity cells and correct for sensor drift. Discrete dissolved oxygen measurements were made with a Lamont-Doherty Earth Observatory (LDEO) amperometric oxygen titration system [*Culberson and Huang*, 1987]. Based on standards and replicate analyses, analytical precision was ± 0.01 ml l^{-1}. Several discrete samples for each cast were used to calibrate the CTD oxygen sensor.

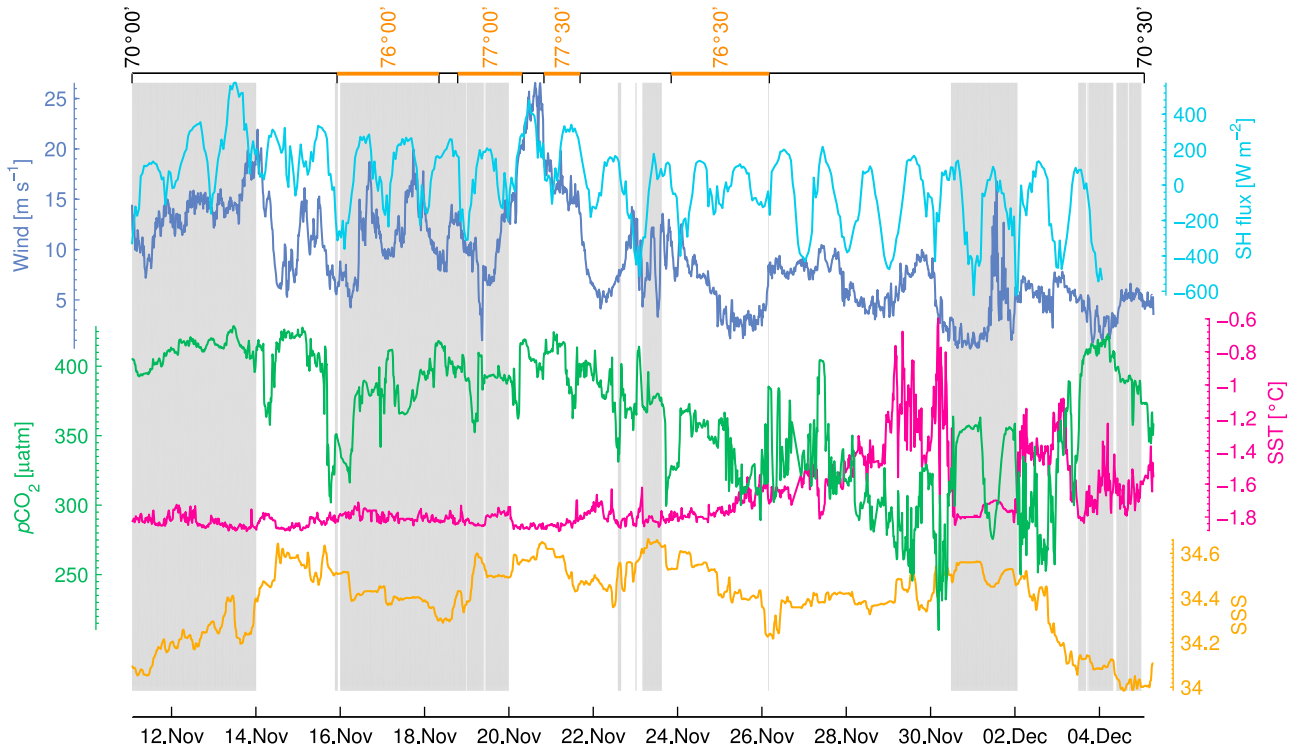

Figure 2. Underway observations of wind, sea surface pCO_2, salinity (SSS), and temperature (SST) during NBP06-08 for the time when the ship was below 70°S. Surface heat flux (SH flux) was computed from bulk formulae (positive upward). Background shading shows sea ice presence/absence (white = open water) computed from SSM/I brightness temperatures using the algorithm of *Markus and Burns* [1995] and interpolated to the cruise track. Top axis shows the four transects discussed in this paper, as well as the crossings of ~70°S.

[11] Observations of sea surface (~5 m) temperature, fluorescence, and salinity were logged continuously from the ship's thermosalinograph (SeaBird Model SBE-21), while semi-continuous pCO_2^{sw} was measured using the LDEO underway equilibrator and LI-COR analytical system installed on the *N. B. Palmer* [*Takahashi et al.*, 2010]. Simultaneous measurements of wind speed, air temperature, relative humidity, sea level pressure, short- and long-wave radiation were made using meteorological equipment installed on the ship. Underway variables were averaged into 15-minute temporal bins.

[12] We diagnosed the mixed layer depth from CTD density profiles as the point in the water column where the density (ρ) exceeded the surface density by an incremental difference $\Delta\sigma_\theta$ ($\sigma_\theta = \rho - 1000$ kg m^{-3}). We considered a range of values and use $\Delta\sigma_\theta = 0.05$.

2.2. Hydrographic Observations

[13] When the ship arrived in the Ross Sea continental shelf region during NBP06-08, conditions were representative of the winter-spring transition. The region was predominantly ice covered (Figure 2) and initial profiles show that the water column was weakly stratified and vertically homogenous with respect to salinity, temperature, and oxygen.

[14] Sea ice cleared from the polynya region following a significant wind event, beginning around day 8 of the cruise (Figure 2). As sea ice cleared, rates of change in surface properties increased. For instance, between day 10 and 20 of the cruise the daily-mean pCO_2^{sw} decreased by over 150 μatm (Figure 2). Overall during the cruise, mean oxygen saturation above 50 m increased by 0.7 ± 0.1 percent per day. Air temperatures were consistently below freezing during the cruise, dipping to about −15°C around 14 Nov, and subsequently increasing with a mean trend of 0.25°C d^{-1} for the remainder of the time that the ship was below 70°S. A diurnal cycle is evident in the surface heat flux, with maximal heating occurring near midnight GMT (Figure 2); turbulent heat loss exceeded shortwave input over the daily cycle during the first half of the cruise, leading to net cooling. Sea surface temperature variability was generally low during this period, reflecting net cooling and the thermal inertia provided by sea ice (Figure 2). Steady surface warming was evident, however, in the latter half of the cruise. In spite of this gradual increase in sea surface temperature, no significant temporal trend was observed in sea surface salinity. This fact and the generally cold air temperatures indicate that sea ice clearing occurred predominantly as a result of advection, rather than melting.

[15] Declining pCO_2^{sw} and increasing surface oxygen saturation are indicative of NPP. Air-sea exchange was also of some importance for oxygen, which has a equilibration timescale much shorter than that of CO_2. In addition to temporal change, substantial spatial variability was evident in upper ocean properties. Regions of particularly intense drawdown are evident in pCO_2^{sw}, for instance, involving

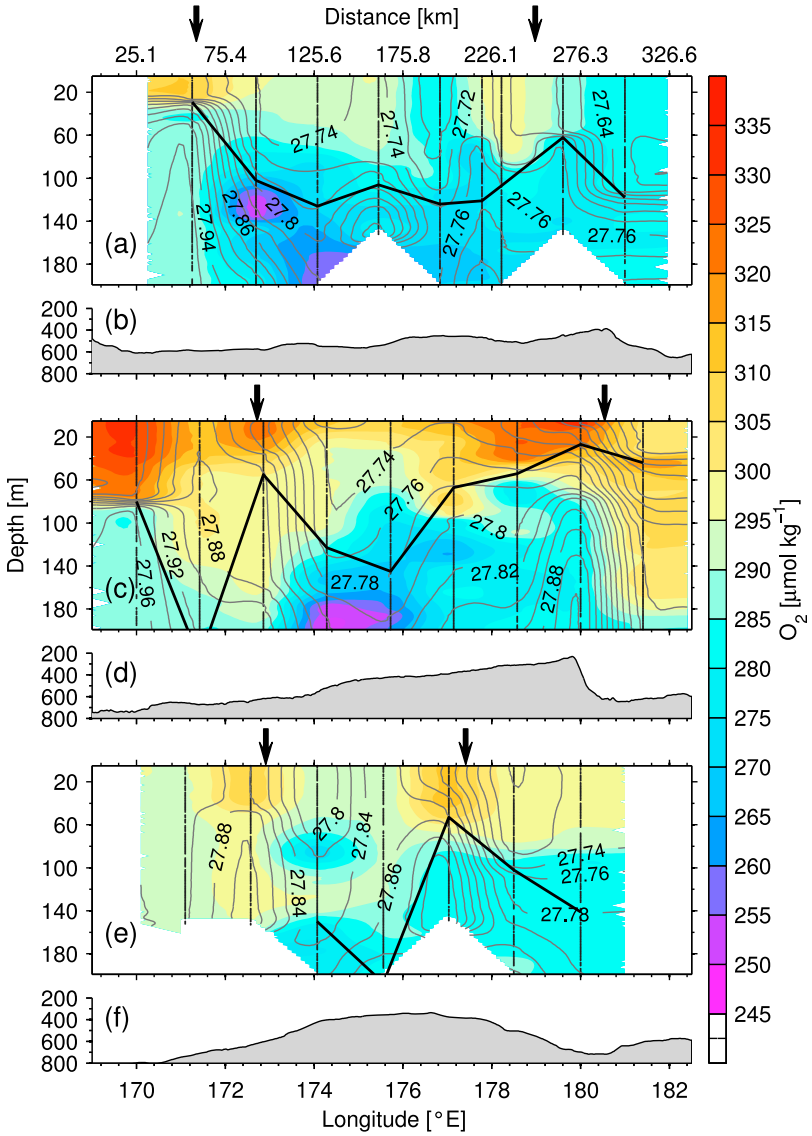

Figure 3. Oxygen, σ_θ, and bathymetry along transects from NBP06-08. (a, c, and e) Gridded oxygen concentration (color) and σ_θ (contours) along 76°S, 76°30′S, and 77°S, respectively. Data were gridded at ~2.5 km × 1 m using a Laplace gradient-minimizing technique. Black vertical lines show locations of observations and the heavy black line shows the mixed layer depth. Density variation over the full depth of the two westernmost casts shown in Figure 3e was less that 0.05 kg m^{-3}. Heavy arrows at the top of each row show the approximate position of fronts discussed in the text. The intense oxygen minima evident in Figures 3a and 3c are likely due to the influence of Modified Circumpolar Deepwater. (b, d, and f) Bathymetry from ETOPO1 [*Amante and Eakins*, 2009] for the section plotted immediately above.

changes of as much as 100 μatm (nearly half the full observed range) over distances of 10 km. Additionally, upper ocean oxygen concentrations varied considerably between casts. It is possible that this type of variability was generated through stirring of lateral gradients in tracers of productivity (i.e., pCO_2^{sw} and oxygen) [*Mahadevan et al.*, 2004; *Resplandy et al.*, 2009], although a tight coupling between underway fluorescence and pCO_2^{sw} ($R = -0.814$, $p < 0.001$), suggests that active biological drawdown played an important role in creating these local gradients. Notably, this tight correlation was not observed during a companion cruise the prior summer; rather, in summer the relationship of active productivity with a drawdown signal was weak due to the time-integrated effect of multiple blooms and horizontal stirring [*Long et al.*, 2011].

2.3. Upper Ocean Fronts

[16] NBP06-08 included four zonal transects, all of which displayed a zonal gradient in surface density, with lighter water found to the east. Underway salinity data (Figure 2) provides a sense of this, noting that all transects except 77°S were occupied from west to east (and the abscissa of Figure 2 is time). Several locations show sharp changes in salinity, indicating the presence of upper ocean fronts. Figure 3 shows gridded oxygen and density structure in the upper 200 m along the three CTD transects (the bottom axis

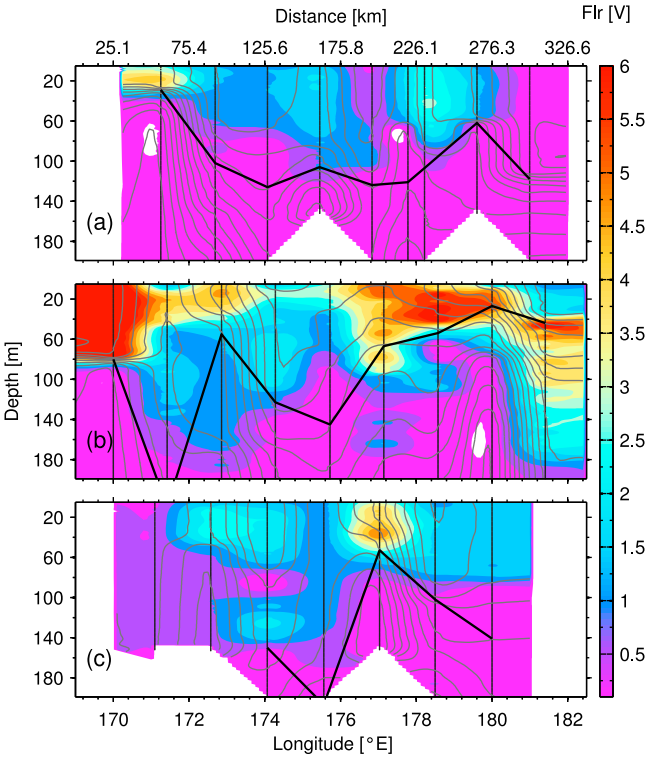

Figure 4. Chlorophyll *a* fluorescence (color) and σ_θ (contours) along (a) 76°S, (b) 76°30′S, and (c) 77°S. Black vertical lines show locations of observations.

on Figure 3 shows longitude, while the top axis shows distance; CTD spacing was about 35 km on average). In each of these transects, two significant fronts are evident, one between about 172°E and 174°E and one close to the dateline. While it is possible that the front might be narrower than depicted on Figure 3, the minimum zonal density gradient at each front is on the order of 10^{-6} kg m^{-4}. A fourth transect, 77°30′S, did not include sufficient CTD casts for gridding (Figure 2); however, a minimum in the surface zonal density gradient of -4×10^{-6} kg m^{-4} indicated a front centered at 176.6°E.

[17] These fronts likely result from the regional mean circulation, which drives a confluence of disparate water masses. This circulation is predominantly barotropic, and hence strongly shaped by variations in bottom topography. Given this fact, it might be expected that the locations of the fronts in the Ross Sea would be linked to features in the bathymetry—and hence would be relatively fixed in time. Indeed, previous observations, most notably *Hales and Takahashi* [2004], documented fronts in locations similar to those described above.

[18] Regardless of formation mechanisms, in situ data from NBP06-08 suggests these fronts play an important role in structuring the spatial distributions of NPP and gas exchange. Indeed, elevated oxygen concentrations were found proximal to fronts, typically slightly west of the maximum surface density gradient in regions of enhanced stratification (Figure 3). There is a temporal component to consider when comparing these sections, since the 76°30′S transect was occupied several days after 76°S (Figure 2). Thus, oxygen concentrations along 76°S are generally lower. However, in each transect, maxima in oxygen concentration coincide with maxima in chlorophyll *a* fluorescence (Figure 4), and a tight relationship is observed between oxygen saturation and fluorescence ($R = 0.929$, $p < 0.001$). Furthermore, satellite images show a correspondence between regions of maximum chlorophyll concentrations and the locations of fronts (Figure 5). Of the two fronts indicated on Figure 5, the eastern one was more clearly diagnosed and persistent in all transects; although its expression at the surface was somewhat variable. Examination of the spatial distribution of chlorophyll reveal that the most intense region of the bloom is immediately west of the location of this front.

[19] In many parts of the world ocean, frontal regions are highly productive due to associated vertical motions that bring nutrient rich water to the surface. In the Ross Sea, macronutrients are replete during the spring phase of the annual bloom. Indeed, during NBP06-08, both nitrate and phosphate were replete, with minimum concentrations of about 22 μmol kg^{-1} and 1.7 μmol kg^{-1}, respectively. Taking 0.5 μmol kg^{-1} as the half-saturation coefficient for nitrate assimilation [*Arrigo et al.*, 2003], these concentrations yield growth rates that are 98% of unlimited growth, indicating a minimal effect of macronutrient limitation. While macronutrients are typically replete in the Ross Sea, iron limitation does play an important role controlling bloom dynamics. Field and modeling studies have suggested that the region becomes iron-limited in summer, at the point when time-integrated Fe export exceeds the seasonal supply [e.g. *Sedwick et al.*, 2000; *Arrigo et al.*, 2003]. Under this paradigm, the region is thought to transition from being primarily light-limited in spring, to Fe limited later in summer. While it is certainly the case that light limitation is important in spring, iron limitation is more complicated. Iron

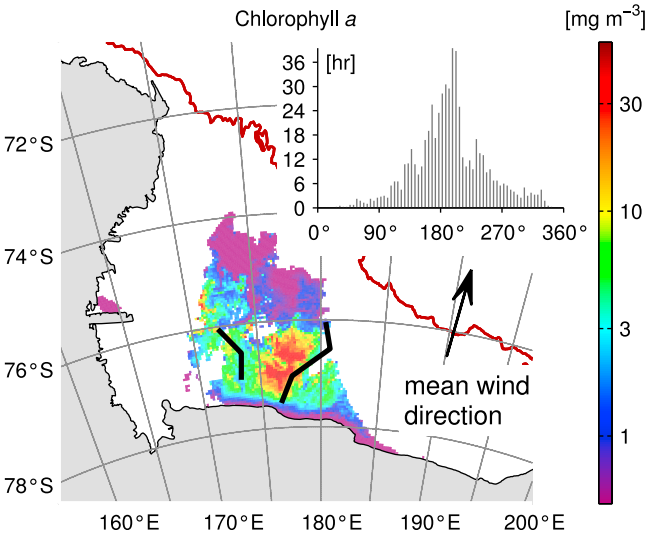

Figure 5. MODIS-Aqua chlorophyll *a* from 28 November 2006. Pixel resolution is 4 km. Black lines show approximate location of upper ocean fronts, as determined by minima in the zonal density gradient. The arrow shows the mean wind direction, while the inset shows a histogram of 15-minute wind direction during NBP06-08, binned at 5°-azimuth intervals.

measurements collected during NBP06-08 show that dissolved Fe concentrations (dFe) in surface waters were low, displaying little spatial variability (0.06 ± 0.04 nM above 40 m, n = 69) [*Sedwick et al.*, 2011]. In spite of ubiquitously low dFe, high primary productivity was observed during the cruise, and satellite data indicated that biomass accumulation continued over the 2006–2007 growing season [*Long et al.*, 2011]. These data suggest that drawdown of dFe may occur earlier in the season than previously believed, and that Fe resupply, either through reduction of particulate Fe or advection, likely plays a role in sustaining the bloom.

[20] The spatial coverage of dFe measurements during NBP06-08 was insufficient to support inferences regarding Fe controls on spatial variability in NPP. Thus, while we cannot rule out Fe limitation as a factor co-limiting phytoplankton growth during NBP06-08, light limitation was certainly important. We hypothesize that shoaling MLs adjacent to fronts led to greater photosynthetic rates, as ML communities were exposed to greater irradiance. We further hypothesize that the decrease in ML depth was caused by Ekman restratification. In the following sections we review the physics behind Ekman restratification; we then test our hypotheses using a numerical model.

3. Ekman Restratification

[21] At wind-forced fronts, Ekman flow can reconfigure the structure of the buoyancy field,

$$b = -g\frac{\rho}{\rho_o};$$

where g is the gravitational acceleration, ρ and ρ_o are the density and reference density, respectively. This process can restratify or destratify the upper ocean depending on the wind direction relative to the orientation of the front.

[22] A measure of the rate at which Ekman advection of buoyancy can re- or destratify the mixed layer is the Ekman buoyancy flux:

$$\mathrm{EBF} = \mathbf{M}_e \cdot \nabla_h b|_{z=0} = \frac{\tau^w}{\rho_o |f|} |\nabla_h b|_{z=0} \cos\theta \qquad (1)$$

where $\mathbf{M}_e$ is the Ekman transport, τ^w is the magnitude of the wind stress, f is the Coriolis parameter, and θ is the angle between the wind stress and the geostrophic shear at the sea surface, which follows the thermal wind balance:

$$\left.\frac{\partial \mathbf{u}_g}{\partial z}\right|_{z=0} = \frac{\hat{k} \times \nabla_h b|_{z=0}}{f},$$

$\hat{k}$ is a unit vector in the vertical [*Thomas and Taylor*, 2010]. Up-front winds, which are directed against the geostrophic shear (i.e. with $90° < \theta < 270°$), result in Ekman advection of waters from the lighter side of the front over waters on the denser side, thereby increasing the stratification [*Thomas and Ferrari*, 2008]. For such winds, the EBF is negative and is thus analogous to a negative (downward) air-sea buoyancy flux caused by heating, precipitation, or ice melt. Both processes restratify the ML. The importance of Ekman advection in modifying the stratification of the upper ocean can therefore be quantified by calculating the relative strengths of the Ekman and air-sea buoyancy fluxes.

[23] In the Ross Sea, the wind was predominantly southerly during the cruise (Figure 5) and hence up-front, suggesting that Ekman advection could be responsible for the local restratification proximal to the fronts. Several questions arise, however; namely: Can Ekman restratification and the EBF compete with mixing and/or restratification associated with 1-D processes driven by air-sea fluxes? Can it explain the lateral variability in stratification observed during NBP06-08? Does Ekman restratification effectively enhance NPP and CO_2 drawdown? In the next section we use numerical experiments to address these questions.

4. Numerical Experiments

[24] While in situ data indicate that fronts are important determinants of the spatial structure in bloom dynamics, quantitative conclusions are difficult to develop from observations alone. The spacing of CTD cast does not sufficiently resolve variability on all relevant scales; furthermore, observations made from a moving platform, during periods exhibiting high rates of temporal change, result in a convolution of space and time. For this reason, we use a numerical model to estimate upper ocean buoyancy budgets and assess the importance of restratification by horizontal advection. The inclusion of a biogeochemical model reveals the tendency of the effect dynamical processes have on NPP and gas exchange, providing insight into the biogeochemical consequences associated with differing dynamical scenarios.

4.1. Model Configurations

[25] We performed a series of idealized numerical experiments designed to represent physical characteristics of the water column and atmospheric forcing observed during the cruise. Our simulations were conducted using the Regional Oceanic Modeling System [ROMS; *Shchepetkin and McWilliams*, 2005], coupled to a biogeochemical model: a modified version of *Fennel et al.* [2006, 2008].

[26] Three simulations were performed: a 1-D experiment with no lateral variability (EXP1), a 2-D run with a spatially-uniform horizontal density gradient (EXP2), and a 2-D simulation with an initial density field set to replicate zonal transects of density collected during NBP06-08 (EXP3). All of the simulations were forced by the observed long/shortwave radiation and air-sea fluxes calculated from ship-based measurements (e.g., Figure 2). The objective of these three experiments was to contrast the evolution of the ML depth and biogeochemistry with and without Ekman advection (EXP2 versus EXP1) and determine to what extent the observed spatial heterogeneity in the stratification and biogeochemistry can be explained by Ekman advection of density, modulated by the zonal variability in the fronts (EXP3).

[27] EXP1 was initialized with a salinity field, S_i, of the form

$$s(z) = \begin{cases} 34.45 - 0.03 \tanh\left(\dfrac{z + 81.13}{28.60}\right) & z \geq -80 \text{ m} \\ 34.38 - 0.0009z & z < -80 \text{ m} \end{cases} \qquad (2)$$

the parameters of which were found by a nonlinear least-squares fit to the mean salinity profile of the first several

casts collected during NBP06-08. For EXP2 a uniform zonal salinity gradient was added to the initial condition: $S_i = s(z) + (\partial\bar{S}/\partial x)x$, where $\partial\bar{S}/\partial x = -3.9 \times 10^{-6}$ psu m^{-1}, a value representative of the fronts in the Ross Sea.

[28] EXP3 was initialized with a salinity field of the form

$$S_i = s(z) + \frac{\partial\bar{S}}{\partial x}x + \sum_{n=1}^{3} a_n \sin\left(\frac{2n\pi x}{L} + \phi_n\right), \tag{3}$$

where L = 300 km. The coefficients in this equation were obtained by fitting equation (3) to the salinity observed on the 76°30′S line at $z = -120$ m (Figure 3b). Resulting in the following: $\partial\bar{S}/\partial x = -1.1 \times 10^{-6}$ psu m^{-1}, $a_1 = -0.11$, $a_2 = -0.03$, $a_3 = -0.05$ psu, $\phi_1 = -0.54$, $\phi_2 = 0.90$, $\phi_3 = 0.55$ rad. The density field from 76°30′S was chosen because this transect had the most clearly developed frontal structures.

[29] For all three experiments the initial temperature, T_i, was uniform and set to −1.8°C, a value representative of the observed hydrography at the beginning of NBP06-08. EXP2 and EXP3 were initialized with a geostrophic meridional velocity, v_i, that satisfied the thermal wind balance: $f\partial v_i/\partial z = -g\beta_s\partial S_i/\partial x$, where $\beta_s = 7.9 \times 10^{-4}$ psu^{-1} is the haline contraction coefficient at T_i. All other components of the velocity were set to zero at the start of each simulation.

[30] In all three experiments vertical mixing was parameterized using the KPP scheme of *Large et al.* [1994]. The depth of the model domain was set to 300 m (200 m for EXP3) with a uniform vertical grid spacing equal to 5 m (4 m for EXP3). The lateral width, L_x, and grid spacing, Δx, of the 2-D experiments was 12 km and 240 m for EXP2, respectively, and L_x = 300 km, Δx = 1 km for EXP3.

[31] Following *Thomas* [2005], the effects of the spatially-uniform lateral density gradient in the 2-D experiments were captured by modifying the equations of motion that ROMS integrates. In doing so, ROMS solves for the perturbation salinity field, i.e. $S - (\partial\bar{S}/\partial x)x$ and periodic lateral boundary conditions can be used for all model variables. All surface forcing fields were spatially uniform.

[32] The biological model uses nitrogen as its primary currency and consists of seven state variables: phytoplankton, zooplankton, nitrate, ammonium, two class sizes of detritus and chlorophyll. We replaced the original parameterization of light limitation used by *Fennel et al.* [2006] with one tuned to represent the Ross Sea ecosystem [*Arrigo and Sullivan*, 1994; *Arrigo et al.*, 2003]. Additionally, to isolate the effect of light availability on NPP, we turned nutrient limitation off by adjusting the half-saturation coefficients for nitrate and ammonium assimilation to very small and large numbers, 1×10^{-6} and 1×10^{6} mmol N m^{-3} respectively. Iron limitation is not represented by the model, thus by turning off macronutrient limitation, we ensure that our results exclusively reflect the effect shoaling ML depths have on alleviating light limitation. Light limited growth rate (μ) under the *Arrigo et al.* [2003] formulation is computed as a function of instantaneous irradiance:

$$\frac{\mu}{\mu_{\max}} = \left[1 - \exp\left(\frac{-I_z}{E_k}\right)\right] R_k \tag{4}$$

where $\mu_{\max}$ is the temperature-dependent maximum growth rate [*Eppley*, 1972], I_z is the depth-dependent photosynthetically usable irradiance (PUR), and E_k is the photoacclimation parameter, represented by

$$E_k = \frac{E_{k,\max}}{1 + 1.7\exp\left(-0.12\langle I_z\rangle_{\lambda_E}\right)} \tag{5}$$

where $E_{k,\max}$ is the maximum value achieved by E_k at high irradiance and $\langle I_z\rangle_{\lambda_E}$ denotes irradiance averaged over some timescale λ_E. Photoinhibition (R_k) is computed as

$$R_k = 1 - \frac{1 - \exp\left(-20\langle I_z\rangle_{\lambda_R}/E_T\right)}{1 + 5 \times 10^{8}\exp\left(-20\langle I_z\rangle_{\lambda_R}/E_T\right)} \tag{6}$$

where E_T is the threshold irradiance, above which photoinhibition limits photosynthesis. $\langle I_z\rangle_{\lambda_R}$ is the mean irradiance over a timescale λ_R. Sensitivity of this parameterization to λ_E and λ_R is minimal in most circumstances [*Long*, 2010]; therefore, we replace $\langle I_z\rangle_{\lambda_E}$ and $\langle I_z\rangle_{\lambda_R}$ with I_z. Additionally, *Arrigo et al.* [2003] compute PUR based on a spectrally-resolved light propagation and adsorption model, resulting in PUR less than total photosynthetically available radiation (PAR). Since *Fennel et al.* [2006] do not resolve light spectrally, we approximate PUR as 0.5 PAR (K. R. Arrigo, personal communication, 2010). I_z is computed as a fraction of shortwave radiation, which is provided at 15 minute intervals to ROMS as forcing data; thus, there is a daily cycle. Light is attenuated with depth in the water column and averaged over each vertical layer. KPP mixes tracers in the boundary layer via turbulent diffusion [*Large et al.*, 1994]; thus, overtime the effect of the mixed layer on photosynthetic rates and biologically-mediated fluxes is captured. Self-shading is implicit in the model, since the attenuation length scale used to compute irradiance at depth is a function of the prognostic chlorophyll concentration.

[33] Phytoplankton, chlorophyll *a*, DIC, dissolved oxygen, and nutrient concentrations were initialized to values representative of the early spring water column in the region [*Long et al.*, 2011]. We used parameters in the biogeochemical model representative of the Ross Sea pelagic ecosystem [*Arrigo et al.*, 2003]; however, our intention is not to fully capture regional ecosystem dynamics, but rather to show the sensitivity of biological rate processes to stratification.

4.2. Evolution of the Near-Surface Stratification: 1-D Versus 2-D Physics

[34] The presence of horizontal density gradients dramatically alters the evolution of the stratification in the Ross Sea. This is most clearly illustrated by contrasting the solutions from the idealized 1-D and 2-D simulations, EXP1 and EXP2, through the use of a buoyancy budget as described below.

[35] A buoyancy budget can be constructed by integrating the buoyancy equation

$$\frac{\partial b}{\partial t} = -\nabla\cdot\left(\mathbf{u}b + \mathbf{F}^b\right) \tag{7}$$

(where $\mathbf{F}^b$ are buoyancy fluxes associated with diabatic processes and/or small-scale turbulence) over a control

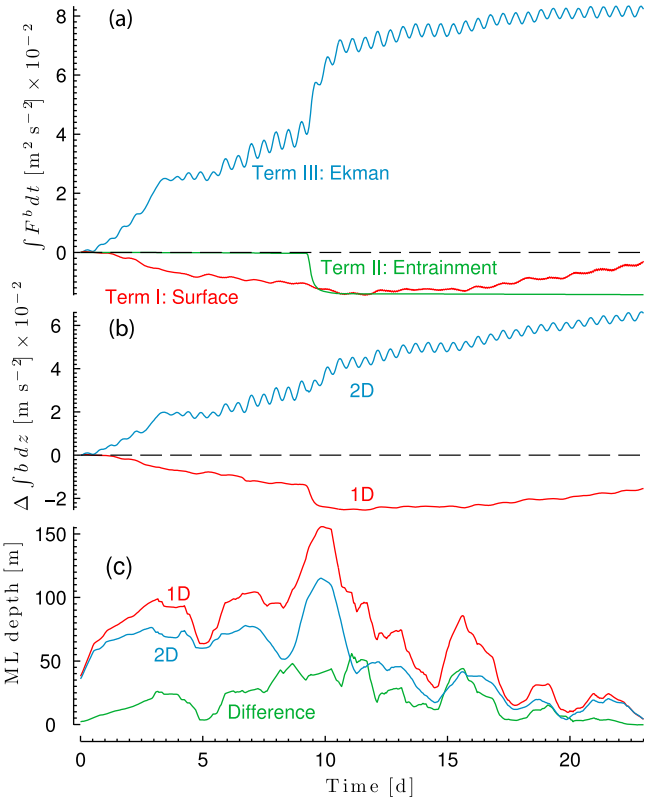

Figure 6. (a) Time-integrated terms in the buoyancy budget for EXP2 (equation (8)). Buoyancy fluxes associated with surface heat exchange (I: $-\bar{F}_{atm}$), the turbulent entrainment of buoyancy at 100 m (II: $\bar{F}_{ent}$) and negative of the Ekman buoyancy flux (III: −EBF). Positive values indicate a tendency to restratify the water column. (b) The net change with respect to time of the buoyancy integrated over the upper 100 m for EXP1 and EXP2. (c) Mixed layer depth in EXP1, EXP2, and the difference (EXP1 − EXP2).

volume. Choosing a control volume that extends over a depth, h, from the sea surface, the buoyancy budget becomes

$$\frac{\partial}{\partial t}\int_{-h}^{0}\bar{b}dz = \underbrace{-\bar{F}^{b}_{atm}}_{\text{I}}\underbrace{+\bar{F}^{b}_{ent}}_{\text{II}}\underbrace{-\int_{-h}^{0}\bar{u}\frac{\partial\bar{b}}{\partial x}dz}_{\text{III}}, \qquad (8)$$

for a buoyancy field with a constant lateral gradient, where the overline denotes a lateral average. In equation (8), terms I and II represent the change in buoyancy due to the air-sea flux of buoyancy, F^{b}_{atm}, and the flux of buoyancy associated with entrainment at $z = -h$, F^{b}_{ent}. At wind-forced fronts, term III is equal to minus the EBF, equation (1), when the depth of integration is deeper than the thickness of the Ekman layer. All three terms in equation (8) were evaluated for EXP2 (F^{b}_{ent} was estimated using the KPP mixing scheme); the time-integral of these are shown in Figure 6a; the time-integral of the left hand side of equation (8) for EXP1 and EXP2 is plotted in Figure 6b.

[36] Surface forcing was identical for 1-D and 2-D simulations. Initially, low air temperatures and high winds caused surface cooling and buoyancy loss in both model configurations (Figure 6a). Wind speed declined during the course of NBP06-08 (Figure 2), resulting in a decrease in the wind-driven turbulent kinetic energy production in the ocean boundary layer. Subsequent to the major decline in wind speed that occurred around day 10, part of the buoyancy lost as a result of surface cooling in the 1-D simulation was recovered by net surface heating (Figure 6). While there was a net loss of buoyancy in the 1-D configuration, the 2-D simulation showed relatively consistent restratification. Comparing the surface and Ekman buoyancy fluxes it can be seen that buoyancy additions resulting from Ekman advection proximal to fronts dwarfed surface heat fluxes (Figure 6a). High frequency fluctuations in the Ekman buoyancy flux (Figure 6a), which are also evident in the total depth-integrated buoyancy of EXP2 (Figure 6b), are caused by inertial oscillations. While Ekman advection consistently leads to restratification in the 2-D configuration, loss of buoyancy due to entrainment can exceed the wind driven buoyancy flux at high wind speed (Figure 6a). The effect of the EBF is evident in ML depths that are consistently shallower in EXP2, relative to EXP1 (Figure 6c).

[37] The evolution of the vertical salinity structure demonstrates the enhanced water column stability that results from Ekman advection (Figure 7). In the 1-D simulation, mixing depths are very responsive to wind speed, thus the pycnocline deepens substantially for the first 10 days of the simulation, resulting in virtually homogenous properties above 100 m (Figure 7a). The loss of surface buoyancy is due primarily to entrainment of more dense water

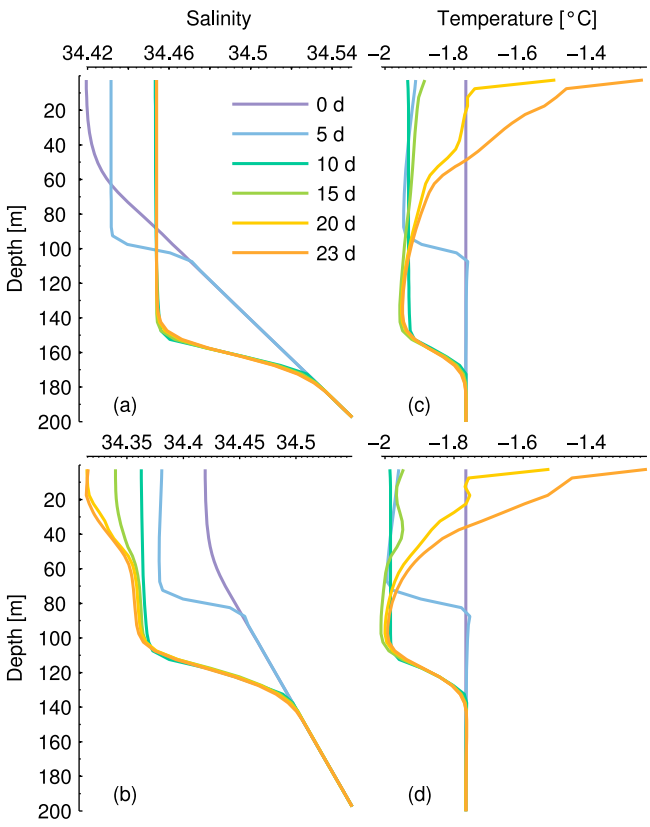

Figure 7. Evolution of vertical salinity and temperature structure for (a and c) EXP1 and (b and d) EXP2. Note differing salinity scales; initial profiles (purple) are identical.

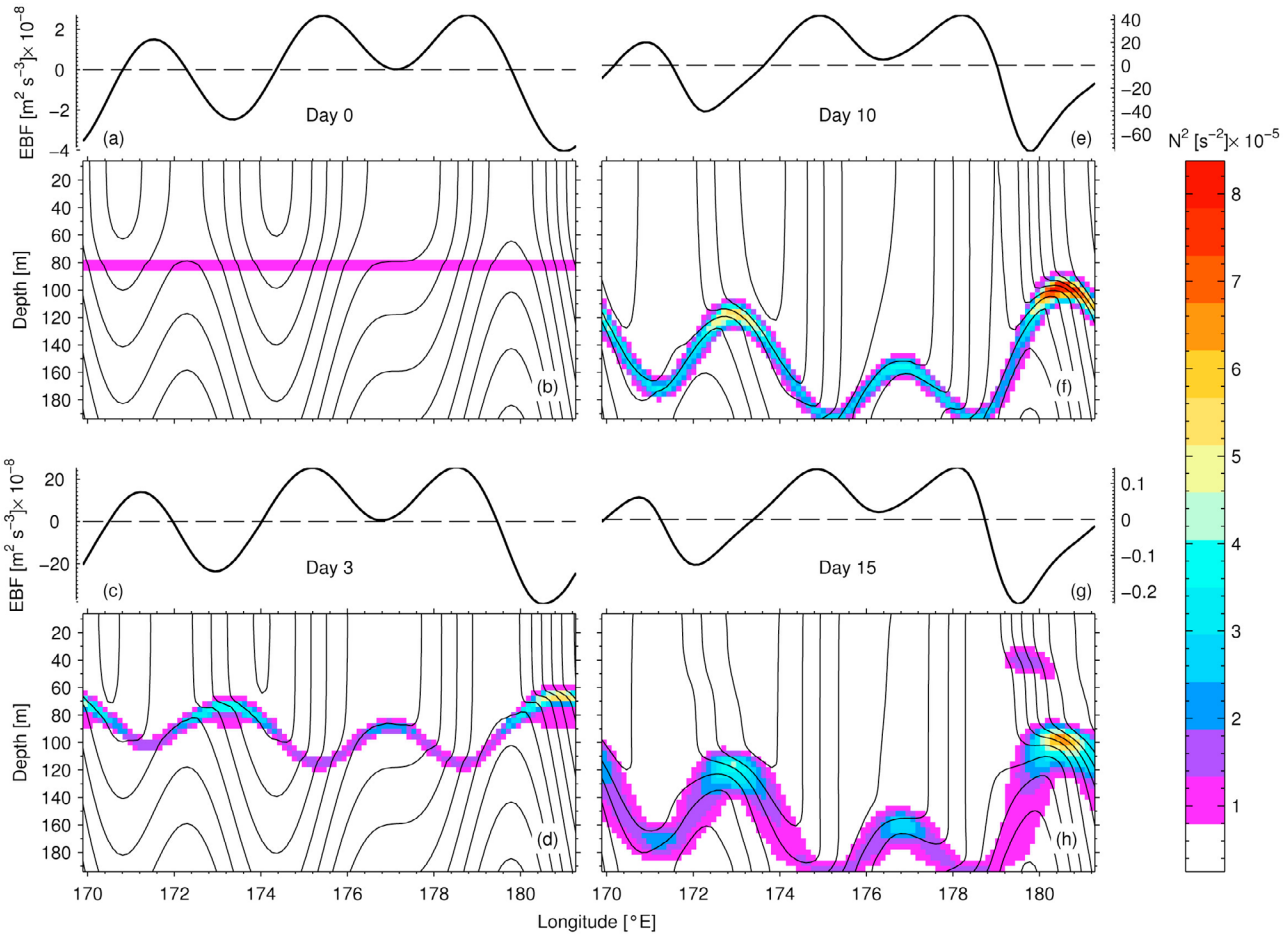

Figure 8. Evolution of the stratification, density, and the Ekman buoyancy flux (EBF) for EXP3. (a, c, e, and g) The EBF for days 0, 3, 10, and 15 of the simulation, respectively; (b, d, f, and h) the corresponding density structure (contours) and N^2 (color).

from below (Figure 6a). Lateral advection in the 2-D model configuration results in consistently increasing stratification, as lighter water from the east moves over more dense water to the west (Figure 7b). Notably, this results in the development of multiple pycnoclines, a feature evident in many CTD profiles from the region.

[38] Enhanced stratification leads to only moderate differences in upper ocean temperature response to surface heating during the latter part of NBP06-08 (Figure 7). After about day 10 of the simulation, buoyancy fluxes due to Ekman advection and surface heating are of similar magnitudes (Figure 6a).

[39] The results of the idealized simulations EXP1 and EXP2 suggest that Ekman advection of density is of first-order importance to the evolution of the stratification in the Ross Sea during early spring. However, a direct comparison of the restratification rates from EXP2 to the observations is not possible because the hydrographic measurements lack a temporal component. Nevertheless, the observations do nominally capture the spatial variability in stratification, which appears to be modulated by fronts (e.g., Figure 4). Therefore, by running a simulation with zonally varying density gradients representative of the region (EXP3) and comparing the spatial structure of the resulting stratification to the observations, we can better assess the role of Ekman restratification in the dynamics of the ML in the Ross Sea. This comparison is described in the next section.

4.3. Spatial Variations in Stratification

[40] The initial condition for density used in EXP3 is shown in Figure 8b. The density gradually decreases from west to east; however, the density gradient is intensified at some locations (near 173.5°, 181°E) and reverses in others (near 175.5°, 179°E). Consequently, for a constant wind vector, the strength and sign of the EBF varies along the transect (Figure 8a). The magnitude of the EBF is modulated over the course of the simulation by time-variable winds, and peaks at $\sim 5 \times 10^{-7}$ m^2 s^{-3} during the period of strong winds between days 9 and 10. To put the magnitude of this number in perspective, this EBF would drive de/restratification at a rate equivalent to cooling/heating the surface ocean by a flux of $\sim$7500 W m^{-2}. Given this strong mixing/restratification potential, it is not surprising that the depth of the ML (evident in depth maxima of N^2, Figure 8) is closely coupled to the zonal structure of the EBF. It should be emphasized that the air-sea fluxes used to force EXP3 were

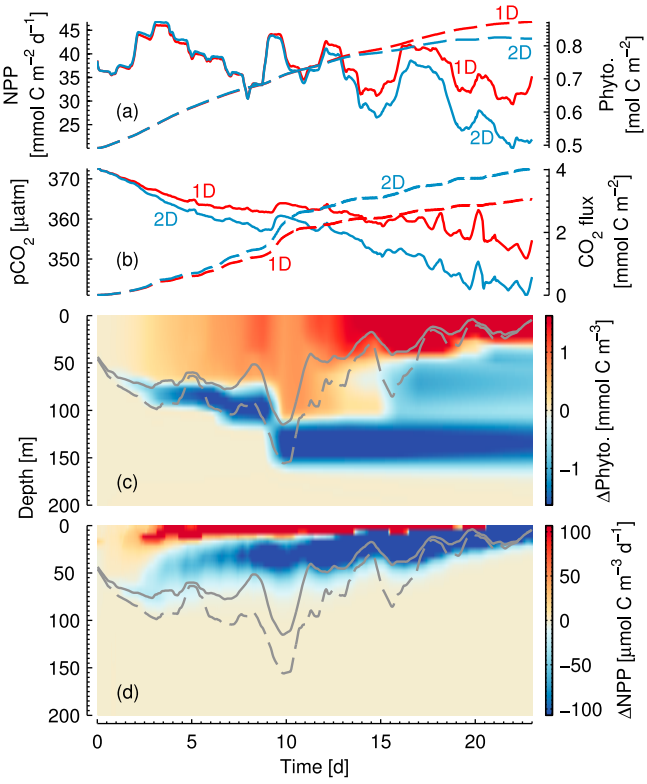

Figure 9. (a) Net primary productivity (NPP; solid lines, left axis) and phytoplankton biomass (dashed line, right axis) in EXP1 (red) and EXP2 (blue). (b) Surface ocean pCO_2 (solid lines, left axis) and time-integrated air-sea CO_2 flux (dashed line, right axis) in EXP1 (red) and EXP2 (blue). (c) Phytoplankton biomass in EXP2 minus that in EXP1. (d) NPP in EXP1 minus that in EXP1. Gray solid and dashed lines in Figures 9c and 9d show the daily-mean mixed layer depth from EXP2 and EXP1, respectively.

spatially uniform: the lateral variations in the ML depth are solely attributable to the modulation of the EBF by multiple fronts.

[41] The shoaling and deepening of the ML in EXP3 between days 9 and 15 (Figure 8h) is qualitatively similar to the zonal variability observed across the 76°30′S line (Figure 4c). In both the observations and model output, the shallowest and deepest MLs are found near 180° and 175°E, respectively. Where winds were oriented up-front and the ML depth is shallowest (the front near 180°E), pycnoclines were observed at $z \approx -80$ m and depths shallower than 40 m (Figure 3b). The model reproduces this phenomenon at the same front in EXP3 (Figure 8), and demonstrates that multiple maxima in stratification intensity form as a result of surface intensified Ekman advection of lighter water over dense—particularly during the strong wind event. The magnitude of the resulting stratification in these pycnoclines: $1 \times 10^{-5} < N^2 < 5 \times 10^{-5}$ s^{-2}, is consistent with the observations at this location.

[42] Based on these findings we can conclude that Ekman advection of density is effective at shaping the structure of the water column in the Ross Sea. In the next section we will examine how this physical mechanisms affects the biogeochemistry of the region.

5. Biogeochemical Implications

[43] Results from EXP1 and EXP2 demonstrate that Ekman restratification enhances NPP in the surface ocean, resulting in greater accumulation of biomass and CO_2 drawdown (Figure 9). Since nutrient limitation and grazing were turned off in our simulations, differences between EXP1 and EXP2 are purely a function of changes in light limitation.

[44] When integrated over the upper 200 m, rates of NPP in EXP1 and EXP2 are quite comparable for the first half of the simulation (Figure 9a). However, the depth distribution of NPP is significantly different between the two experiments. EXP2 has higher rates of NPP in the surface above 25 m (Figure 9d) leading to compounding gains in phytoplankton biomass in this region (Figure 9c). In contrast, the distribution of phytoplankton is more vertically uniform in EXP1, and extends over a greater depth than in EXP2. Thus, phytoplankton biomass (Figure 9c), and hence NPP (Figure 9d), is actually greater at depth in EXP1 versus EXP2.

[45] In both EXP1 and EXP2, transient rates of NPP track fluctuations in ML depth—the correlation is positive ($R = 0.606$, $p < 0.001$), in the sense that ML deepening results in increased depth-integrated NPP (Figures 9a and 9d). As the ML deepens, phytoplankton biomass is distributed over a larger volume. This has the effect of diluting chlorophyll concentrations, a primary determinant of the light attenuation length-scale; thus, as MLs deepen, light penetration also increases, thereby increasing biomass-normalized irradiance exposure and depth-integrated rates of NPP. These effects are clearly evident in Figure 9c, which shows the biomass difference between EXP2 and EXP1. The high wind event on day 10 resulted in ML deepening in both experiments, mixing phytoplankton biomass to greater depths in the water column. As MLs subsequently shoaled, phytoplankton were stranded at depth. Since the ML in EXP1 was deeper on day 10, EXP2 showed a large negative biomass anomaly (relative to EXP1) at about 150 m; this anomaly persisted for the remainder of the simulation (Figure 9c). After the day-10 event, the difference in ML depth between EXP1 and EXP2 diminished. Since biomass was more dilute in EXP1, depth-integrated rates of NPP exceeded those in EXP2, where high chlorophyll biomass in the surface resulted in self-shading of the bloom at depth.

[46] While the vertical integral of NPP was very similar between the two experiments, particularly during the first half of the simulation, the impact of NPP on air-sea CO_2 exchange is greater in EXP2. Due to shallower MLs, NPP is concentrated within a smaller ML volume in EXP2; thus, the proportional effect on CO_2 drawdown is greater, which results in lower pCO_2^{sw} and enhanced atmosphere-to-ocean CO_2 transfer (Figure 9b).

[47] Variance in biogeochemical fields reflects a coupling between physical and biological processes. As we have just seen, the ML depth modulates biological rate processes and surface drawdown; this will generate variance in biogeochemical fields at the scales over which ML depths vary.

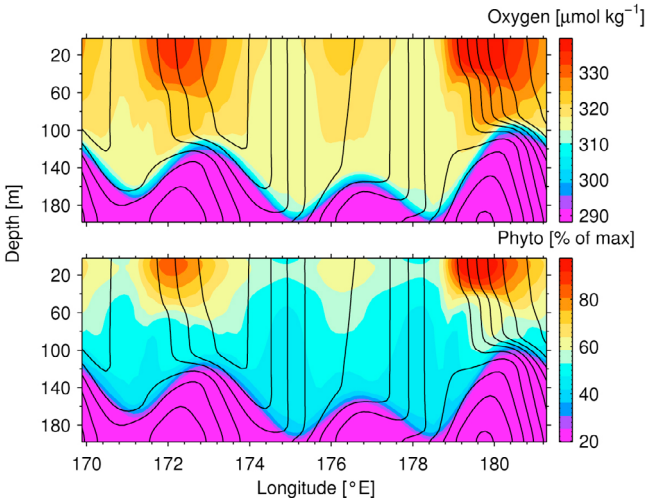

Figure 10. (top) Oxygen and (bottom) phytoplankton concentrations from day 14 of EXP3, which roughly corresponds to the midpoint of the 76°30′S line occupation. The contour lines show the isopycnals plotted in Figure 8. The variability in oxygen concentration agrees well with the observations, with the exception of the oxygen minimum at ∼174.5°E. This feature is likely due to the influence of MCDW, a component not included in the model. Phytoplankton are plotted as percent of the maximum to facilitate comparison with the fluorescence data (Figure 4b).

Once lateral and vertical gradients are established, redistribution by horizontal stirring imparts additional variance to the structure of biogeochemical fields [*Mahadevan et al.*, 2004; *Resplandy et al.*, 2009]. EXP3 provides some insight into how these mechanisms operate in the early-season Ross Sea. The simulation was initialized with spatially uniform biogeochemical fields, including phytoplankton biomass, DIC, and dissolved oxygen. Initially, the primary mechanism generating variability in these fields is NPP in the surface ML. Where NPP is high, oxygen and phytoplankton biomass accumulation is enhanced—accompanied by drawdown of DIC and nutrients. Strong productivity signals are found where the EBF produced shoaling mixed layers (Figure 10). The zonal pattern of oxygen and phytoplankton biomass (Figure 10), as well as the overall variance, is consistent with that observed along 76°30′ (Figures 3b and 4b, respectively).

[48] Since the EBF is enhanced at fronts, there is a tight coupling of variability in surface drawdown to the zonal density structure (Figure 11a), particularly at the beginning

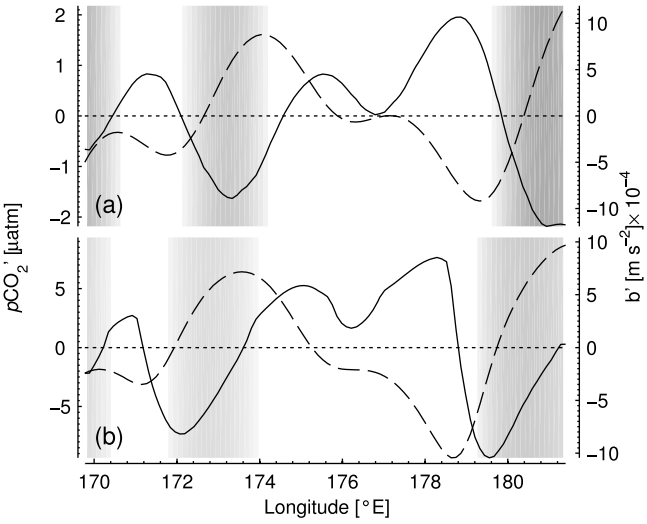

Figure 11. Zonal anomaly of sea surface pCO_2 (black line, left axes) and sea surface buoyancy (dashed lines, right axes) from EXP3 at (a) day 3 and (b) day 15. Background shading indicates the relative magnitude of the time-averaged Ekman buoyancy flux (⟨EBF⟩), with darker colors corresponding to more negative values ($-1.4 \times 10^{-7} \leq \langle \mathrm{EBF} \rangle \leq 0$ m^2 s^{-3}), indicative of a greater restratification contribution (equation (1)). White areas indicate ⟨EBF⟩ > 0.

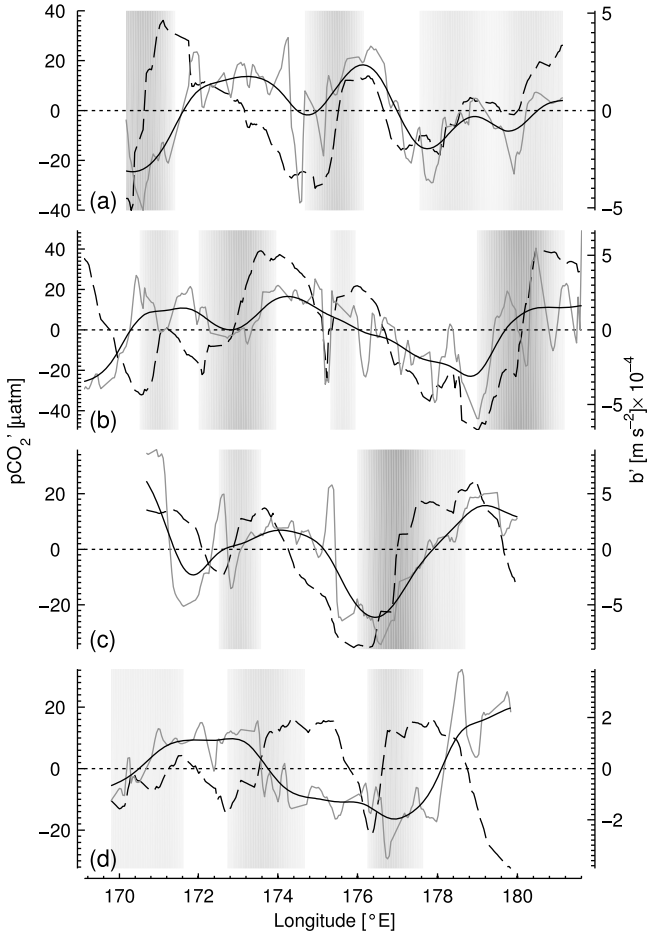

Figure 12. Zonal anomaly of sea surface pCO_2 (black = smoothed and gray lines, left axes) and sea surface buoyancy data (dashed lines, right axes) for transects (a) 76°S, (b) 76° 30′S, (c) 77°S and (d) 77°30′S.Data were binned at 1 km resolution and the zonal trend was subtracted. pCO_2^{sw} data were smoothed using a Gaussian kernel low-pass filter with a 10 km bandwidth. Background shading indicates the relative magnitude of the time-averaged Ekman buoyancy flux (⟨EBF⟩), with darker colors corresponding to more negative values ($-9.7 \times 10^{-8} \leq \langle \mathrm{EBF} \rangle \leq 0$ m^2 s^{-3}), indicative of a greater restratification contribution (equation 1). White areas indicate ⟨EBF⟩ > 0.

of EXP3. As the simulation progresses, vertical gradients in DIC, oxygen, and nutrients develop. These can be exploited by mixing to enhance spatial variability. Vertical mixing is strongest where winds are oriented down-front, bringing deep water that is DIC-rich/O_2-poor to the surface. This phenomenon is responsible for high DIC/pCO_2 anomalies at ~175° and ~178°E, late in EXP3 (Figure 11b).

[49] Underway measurements collected during NBP06-08 display patterns consistent with EXP3. Figure 12 shows pCO_2^{sw} and sea surface buoyancy data along each of the four transects. The magnitude of pCO_2^{sw} drawdown is underestimated in the model. This may be a result of underestimating NPP as well drawdown occurring prior to the start of the simulation. In general, pCO_2^{sw} observations display significantly more short length scale variability than the observed buoyancy field. However, on scales of about 10 km, pCO_2^{sw} is closely coupled to the structure of the zonal buoyancy field along each transect, except 77°30′S. This latter transect is very close to the Ross Ice Shelf (Figure 1) and thus may have different atmospheric and oceanic dynamics. While the precise phasing of the relationship between pCO_2^{sw} and the zonal buoyancy gradient is complicated by space-time convolution in the observations, the overall correspondence further reinforces the notion that Ekman restratification is of primary importance in generating spatial variability in pCO_2^{sw}.

[50] Sign changes in the EBF generate deep and shallow mixed layers in close proximity. These in turn produce abrupt spatial variations in surface drawdown, with implications for air-sea fluxes. Since the water column is initially undersaturated with respect to oxygen, re-saturation occurs via both gas exchange and biological oxygen production. In contrast, the water column is initially supersaturated with respect to CO_2, but weak buffering (high Revelle Factor) means that minimal NPP is required to lower pCO_2^{sw} below atmospheric saturation. Thus, for the entire duration of EXP3 (and NBP06-08), the ocean was a sink for both CO_2 and oxygen. However, since NPP produces oxygen, thereby diminishing the gradient driving air-sea exchange, oxygen flux is reduced where NPP is greatest, where ML depths are shallow. The opposite is true for CO_2: ocean uptake of CO_2 is enhanced by Ekman restratification.

6. Discussion

[51] The numerical experiments demonstrate that Ekman restratification can shoal MLs and alleviate light limitation, thereby stimulating NPP and surface drawdown proximal to upper ocean fronts. While the patterns of variability produced by the idealized models are consistent with those observed in situ, there are other mechanisms that can drive restratification of the upper ocean near fronts. Frontogenesis and baroclinic instabilities in the ML, known as ML instabilities (MLIs), are two such processes not captured in our 2-D simulations; it is possible that these contributed to the shoaling of the MLs during NBP06-01. We will describe both of these mechanisms in turn and estimate scalings for the restratification they induce relative to Ekman advection.

[52] Frontogenesis occurs when confluent flow, in the presence of lateral density variability, results in local intensification of horizontal density gradients. To maintain the along-front flow in geostrophic balance, frontogenesis induces an overturning circulation in the cross-front plane, in the sense so as to flatten isopycnals and hence increase stratification [*Lapeyre et al.*, 2006]. MLIs are a form of baroclinic instability that derive kinetic energy from the available potential energy (APE) associated with the tilted isopyncnals of fronts in the mixed layer [*Fox-Kemper et al.*, 2008]. As MLIs release APE, they drive a net overturning motion that causes isopyncals to slump (become more horizontal) and the ML to restratify. These processes restratify the ML through differential horizontal advection of density; thus, they induce restratification at a rate proportional to the strength of their respective cross-front velocities.

[53] *Thomas and Ferrari* [2008] derived scalings for the cross-front velocities associated with frontogenesis (U_{fr}) and Ekman advection (U_{ek}): $U_{fr} = (\alpha/f)\Delta v_g$, and $U_{ek} = \sqrt{\tau^w/\rho_o}$, respectively, where α is a measure of the strain associated with the confluent flow that drives frontogenesis and $\Delta v_g = (H/f)\partial b/\partial x$ is the change in the geostrophic flow across the ML of depth H (x is the cross-front direction). *Fox-Kemper et al.* [2008] showed that restratification by MLIs could be parameterized using a cross-front velocity of strength $U_{MLI} = C_e \Delta v_g$, where $C_e = 0.06$. Using the properties of the fronts and wind-forcing observed in the Ross Sea, we estimate values for U_{fr}, U_{ek}, and U_{MLI} below.

[54] Surface currents in the Ross Sea have speeds on the of order 0.1 m s^{-1} and vary over distances typically greater than 10 km [*Van Woert et al.*, 2003; *Assmann et al.*, 2003]. Thus, we would expect the frontogenetic strain, α, in the region to be weaker than 0.1f. Given the magnitude of the zonal buoyancy gradients at the fronts of $\mathcal{O}(1 \times 10^{-8}$ s$^{-2})$ as estimated using the high-resolution underway data, and ML depths of $\mathcal{O}$(100 m) (e.g., Figures 3 and 12) the change in the geostrophic flow across the ML is $\Delta v_g \sim 0.01$ m s^{-1}. The cross-front velocities associated with frontogenesis and MLIs are thus estimated to be of order $U_{fr} \sim U_{MLI} \sim 0.001$ m s^{-1}. During NBP06-08, the wind stress ranged from $0.1 < \tau^w < 2$ N m^{-2}, yielding an Ekman flow $0.01 < U_{ek} < 0.05$ m s^{-1}.

[55] While subject to uncertainty associated with the assumptions outlined above, these scaling calculations suggest that Ekman advection should restratify the ML at a rate that is at least an order of magnitude larger than that associated with frontogenesis or ML eddies and thus these three-dimensional processes are likely of secondary importance to the evolution of the ML in the Ross Sea. This is in contrast to other regions of the ocean where eddy-driven restratification has been found to enhance NPP and modulate the onset of the spring bloom [e.g *Lévy et al.*, 2000]. The dominance of Ekman restratification in the Ross Sea is a consequence of the strong atmospheric forcing and relatively weak fronts (and hence eddy velocities) of the region.

7. Conclusion

[56] We have presented observations collected during the spring phase of the annual phytoplankton bloom in the Ross Sea. These data show biogeochemical signals associated with NPP concentrated near upper ocean fronts. Frontal regions were also observed to have enhanced upper water column stratification. Since NPP in spring is responsive to enhanced light availability, which increases as ML depths shoal, the correspondence between stratification and NPP

makes sense. However, the mechanisms generating stratification could not be accounted for by traditional 1-D ML models.

[57] The Ross Sea region is characterized by a significant background zonal buoyancy gradient. Fronts occur as local intensifications of this gradient and tend to be aligned with continental shelf topography. Predominantly southerly winds result in the tendency for Ekman advection to move less dense water from the east over denser water to the west. Using idealized simulations, we demonstrate that this mechanism, Ekman restratification, drives shoaling MLs and stimulates NPP via alleviation of light limitation. The idealized models produce patterns of variability in biogeochemical tracers that are consistent with those observed in situ.

[58] Ekman restratification is dependent on the strength and direction of lateral buoyancy gradients with respect to the orientation of wind-forcing; thus, given a prevailing wind direction, the spatial structure of variability in ML depth is tied to the location of fronts. Enhanced stratification leads to higher rates of NPP due to greater light availability. Higher rates of NPP result in more intense drawdown of surface DIC and nutrients, as well as accumulation of oxygen. Greater carbon drawdown and oxygen accumulation enhances air-sea exchange of CO_2 and accelerates oxygen re-saturation. The location of fronts, therefore, is an important determinant of the spatial distribution of NPP and important biogeochemical fluxes early in the growing season in the Ross Sea. Given that fronts in the Ross Sea are linked to bathymetry, this mechanism explains in part the location of recurring blooms. Furthermore, interannual variability in wind direction and intensity can modulate the magnitude of seasonal NPP.

[59] Continental shelf seas surrounding Antarctica play an important role in the global carbon cycle. Surface processes in these regions determine the chemical composition of the deep ocean. Accurately representing the processes affecting stratification, rates of NPP, and air-sea exchange is thus important to resolving the global ocean carbon cycle. In order to accurately capture seasonal transitions and the effect of spatial variability in productivity and air-sea exchange, oceanographic models must represent processes occurring at upper ocean fronts. It should be noted that fronts are ubiquitous in the upper ocean. Therefore it is likely that restratification of the ML by Ekman flows and other frontal processes is important in the dynamics of early season phytoplankton blooms in other high-latitude regions that are nutrient replete, yet light-limited.

[60] **Acknowledgments.** This work was supported by the US NSF (OPP 0338350 to RDB). We thank the captain and crew of the *Nathaniel B. Palmer*. The comments of two anonymous reviewers greatly improved this manuscript.

References

Amante, C., and B. W. Eakins (2009), ETOPO1 1 arc-minute global relief model: Procedures, data sources and analysis, *NOAA Tech. Memo. NESDIS NGDC-24*, Natl. Geophys. Data Cent., Dep. of Commer., Boulder, Colo.

Arrigo, K. R., and C. W. Sullivan (1994), A high resolution bio-optical model of microalgal growth: Tests using sea-ice algal community time-series data, *Limnol. Oceanogr.*, *39*(3), 609–631.

Arrigo, K., and G. van Dijken (2004), Annual changes in sea-ice, chlorophyll a, and primary production in the Ross Sea, Antarctica, *Deep Sea Res., Part II*, *51*(1-3), 117–138.

Arrigo, K. R., and G. L. van Dijken (2007), Interannual variation in air-sea CO_2 flux in the Ross Sea, Antarctica: A model analysis, *J. Geophys. Res.*, *112*, C03020, doi:10.1029/2006JC003492.

Arrigo, K. R., D. L. Worthen, and D. H. Robinson (2003), A coupled ocean-ecosystem model of the Ross Sea: 2. Iron regulation of phytoplankton taxonomic variability and primary production, *J. Geophys. Res.*, *108*(C7), 3231, doi:10.1029/2001JC000856.

Arrigo, K. R., G. van Dijken, and M. C. Long (2008), Coastal Southern Ocean: A strong anthropogenic CO_2 sink, *Geophys. Res. Lett.*, *35*, L21602, doi:10.1029/2008GL035624.

Assmann, K., H. H. Hellmer, and A. Beckmann (2003), Seasonal variation in circulation and water mass distribution on the Ross Sea continental shelf, *Antarct. Sci.*, *15*, 3–11.

Bates, N. R., D. A. Hansell, C. A. Carlson, and L. I. Gordon (1998), Distribution of CO_2 species, estimates of net community production, and air-sea CO_2 exchange in the Ross Sea polynya, *J. Geophys. Res.*, *103*(C2), 2883–2896.

Canadell, J. G., et al. (2007), Contributions to accelerating atmospheric CO_2 growth from economic activity, carbon intensity, and efficiency of natural sinks, *Proc. Natl. Acad. Sci. U. S. A.*, *104*(47), 18,866–18,870.

Culberson, C. H., and S. Huang (1987), Automated amperometric oxygen titration, *Deep Sea Res., Part A*, *34*(5–6), 875–880.

Eppley, R. W. (1972), Temperature and phytoplankton growth in the sea, *Fish. Bull.*, *70*(4), 1063–1085.

Fennel, K., J. Wilkin, J. Levin, J. Moisan, J. O'Reilly, and D. Haidvogel (2006), Nitrogen cycling in the Middle Atlantic Bight: Results from a three-dimensional model and implications for the North Atlantic nitrogen budget, *Global Biogeochem. Cycles*, *20*, GB3007, doi:10.1029/2005GB002456.

Fennel, K., J. Wilkin, M. Previdi, and R. Najjar (2008), Denitrification effects on air-sea CO_2 flux in the coastal ocean: Simulations for the northwest North Atlantic, *Geophys. Res. Lett.*, *35*, L24608, doi:10.1029/2008GL036147.

Fox-Kemper, B., R. Ferrari, and R. Hallberg (2008), Parameterization of mixed layer eddies. Part I: Theory and diagnosis, *J. Phys. Oceanogr.*, *38*(6), 1145–1165.

Franks, P., and L. Walstad (1997), Phytoplankton patches at fronts: A model of formation and response to wind events, *J. Mar. Res.*, *55*(1), 1–29.

Hales, B., and T. Takahashi (2004), High-resolution biogeochemical investigation of the Ross Sea, Antarctica, during the AESOPS (U. S. JGOFS) Program, *Global Biogeochem. Cycles*, *18*, GB3006, doi:10.1029/2003GB002165.

Ito, T., and M. Follows (2005), Preformed phosphate, soft tissue pump and atmospheric CO_2, *J. Mar. Res.*, *63*(4), 813–839.

Jones, H., and J. Marshall (1997), Restratification after deep convection, *J. Phys. Oceanogr.*, *27*(10), 2276–2287.

Kraus, E., and J. Turner (1967), A one-dimensional model of the seasonal thermocline: II. The general theory and its consequences, *Tellus*, *19*(1), 98–105.

Kwok, R. (2005), Ross Sea ice motion, area flux, and deformation, *J. Clim.*, *18*(18), 3759–3776.

Lapeyre, G., P. Klein, and B. L. Hua (2006), Oceanic restratification forced by surface frontogenesis, *J. Phys. Oceanogr.*, *36*, 1577–1590.

Large, W. G., J. C. McWilliams, and S. C. Doney (1994), Oceanic vertical mixing: A review and a model with a nonlocal boundary layer parameterization, *Rev. Geophys.*, *32*(4), 363–403, doi:10.1029/94RG01872.

Le Quéré, C., et al. (2009), Trends in the sources and sinks of carbon dioxide, *Nat. Geosci.*, *2*, 831–836.

Lévy, M., M. Visbeck, and N. Naik (1999), Sensitivity of primary production to different eddy parameterizations: A case study of the spring bloom development in the northwestern Mediterranean Sea, *J. Mar. Res.*, *57*(3), 427–448.

Lévy, M., L. Mémery, and G. Madec (2000), Combined effects of mesoscale processes and atmospheric high-frequency variability on the spring bloom in the MEDOC area, *Deep Sea Res., Part I*, *47*(1), 27–53.

Long, M. C. (2010), Upper ocean physical and ecological dynamics in the Ross Sea, Antarctica, Ph.D. thesis, Stanford Univ., Stanford, Calif.

Long, M. C., R. B. Dunbar, P. D. Tortell, W. O. Smith, D. A. Mucciarone, and G. R. DiTullio (2011), Vertical structure, seasonal drawdown, and net community production in the Ross Sea, Antarctica, *J. Geophys. Res.*, *116*, C10029, doi:10.1029/2009JC005954.

Mahadevan, A., M. Lévy, and L. Mémery (2004), Mesoscale variability of sea surface pCO_2: What does it respond to?, *Global Biogeochem. Cycles*, *18*, GB1017, doi:10.1029/2003GB002102.

Marinov, I., A. Gnanadesikan, J. R. Toggweiler, and J. L. Sarmiento (2006), The Southern Ocean biogeochemical divide, *Nature*, *441*(7096), 964–967.

Markus, T., and B. A. Burns (1995), A method to estimate subpixel-scale coastal polynyas with satellite passive microwave data, *J. Geophys. Res.*, *100*, 4473–4487, doi:10.1029/94JC02278.

Orsi, A. H., and C. L. Wiederwohl (2009), A recount of Ross Sea waters, *Deep Sea Res. Part II*, *56*(13-14), 778–795.

Orsi, A. H., W. M. Smethie Jr., and J. L. Bullister (2002), On the total input of Antarctic waters to the deep ocean: A preliminary estimate from chlorofluorocarbon measurements, *J. Geophys. Res.*, *107*(C8), 3122, doi:10.1029/2001JC000976.

Oschlies, A. (2002), Improved representation of upper-ocean dynamics and mixed layer depths in a model of the North Atlantic on switching from eddy-permitting to eddy-resolving grid resolution, *J. Phys. Oceanogr.*, *32*(8), 2277–2298.

Price, J. F., R. A. Weller, and R. Pinkel (1986), Diurnal cycling: Observations and models of the upper ocean response to diurnal heating, cooling, and wind mixing, *J. Geophys. Res.*, *91*(C7), 8411–8427, doi:10.1029/JC091iC07p08411.

Resplandy, L., M. Lévy, F. d'Ovidio, and L. Merlivat (2009), Impact of submesoscale variability in estimating the air-sea CO_2 exchange: Results from a model study of the POMME experiment, *Global Biogeochem. Cycles*, *23*, GB1017, doi:10.1029/2008GB003239.

Sabine, C. L., et al. (2004), The oceanic sink for anthropogenic CO_2, *Science*, *305*(5682), 367–371.

Sandrini, S., N. Ait-Ameur, P. Rivaro, S. Massolo, F. Touratier, L. Tositti, and C. Goyet (2007), Anthropogenic carbon distribution in the Ross Sea, Antarctica, *Antarct. Sci.*, *19*(3), 395–407.

Sedwick, P. N., G. R. DiTullio, and D. J. Mackey (2000), Iron and manganese in the Ross Sea, Antarctica: Seasonal iron limitation in Antarctic shelf waters, *J. Geophys. Res.*, *105*(C5), 11,321–11,336, doi:10.1029/2000JC000256.

Sedwick, P. N., et al. (2011), Early-season depletion of dissolved iron in the Ross Sea polynya: Implications for iron dynamics on the Antarctic continental shelf, *J. Geophys. Res.*, *116*, C12019, doi:10.1029/2010JC006553.

Shchepetkin, A. F., and J. C. McWilliams (2005), The regional oceanic modeling system (ROMS): A split-explicit, free-surface, topography-following-coordinate oceanic model, *Ocean Modell.*, *9*(4), 347–404.

Sweeney, C. (2003), The annual cycle of surface water CO_2 and O_2 in the Ross Sea: A model for gas exchange on the continental shelves of Antarctica, in *Biogeochemistry of the Ross Sea*, *Antarct. Res. Ser.*, vol. 78, edited by G. R. DiTullio and R. Dunbar, pp. 295–312, AGU, Washington, D. C.

Sweeney, C., D. A. Hansell, C. A. Carlson, L. A. Codispoti, L. I. Gordon, J. Marra, F. J. Millero, W. O. Smith, and T. Takahashi (2000), Biogeochemical regimes, net community production and carbon export in the Ross Sea, Antarctica, *Deep Sea Res. Part II*, *47*(15-16), 3369–3394, doi:10.1016/S0967-0645(00)00072-2.

Tagliabue, A., and K. Arrigo (2005), Iron in the Ross Sea: 1. Impact on CO_2 fluxes via variation in phytoplankton functional group and non-Redfield stoichiometry, *J. Geophys. Res.*, *110*, C03009, doi:10.1029/2004JC002531.

Takahashi, T., S. C. Sutherland, and A. Kozyr (2010), Global ocean surface water partial pressure of CO_2 database: Measurements performed during 1957–2009 (Version 2009), http://cdiac.ornl.gov/ftp/oceans/LDEO_Database/Version_2009/, Carbon Dioxide Inf. Anal. Cent., Oak Ridge Natl. Lab., U.S. Dep. of Energy, Oak Ridge, Tenn., doi:10.3334/CDIAC/otg.ndp088(V2009).

Thomas, L. (2005), Destruction of potential vorticity by winds, *J. Phys. Oceanogr.*, *35*(12), 2457–2466.

Thomas, L., and R. Ferrari (2008), Friction, frontogenesis, and the stratification of the surface mixed layer, *J. Phys. Oceanogr.*, *38*(11), 2501–2518.

Thomas, L. N., and J. R. Taylor (2010), Reduction of the usable wind-work on the general circulation by forced symmetric instability, *Geophys. Res. Lett.*, *37*, L18606, doi:10.1029/2010GL044680.

Thomas, L., A. Tandon, and A. Mahadevan (2008), Submesoscale processes and dynamics, in *Ocean Modeling in an Eddying Regime*, *Geophys. Monogr. Ser.*, vol. 177, edited by M. Hecht and H. Hasumi, pp. 17–38, AGU, Washington D. C.

Townsend, D., M. Keller, M. Sieracki, and S. Ackleson (1992), Spring phytoplankton blooms in the absence of vertical water column stratification, *Nature*, *360*(6399), 59–62.

Van Woert, M. L., E. S. Johnson, L. Langone, D. L. Worthen, A. Monaghan, D. H. Bromwich, R. Meloni, and R. B. Dunbar (2003), The Ross Sea circulation during the 1990s, in *Biogeochemistry of the Ross Sea*, *Antarct. Res. Ser.*, vol. 78, edited by G. R. DiTullio and R. Dunbar, pp. 5–34, AGU, Washington, D. C.

R. B. Dunbar and L. N. Thomas, Department of Environmental Earth System Science, Stanford University, 473 Via Ortega, Y2E2 Bldg., Stanford, CA 94305, USA.

M. C. Long, National Center for Atmospheric Research, 1850 Table Mesa Dr., Boulder, CO 80305, USA. (mclong@ucar.edu)